Revision 2 – correction date 24-03-2026

Word Count: 8731

Shielding of periclase by bridgmanite during compression of a polycrystalline mantle assemblage

Viktoria E. Trautner[1,a], Egor Koemets[1,b], Biao Wang[1,c], Niccolo Satta[1,d], Johannes Buchen[1,2], Gareth M. Hughes[3], Estelle E. Ledoux[1], Katharina Marquardt[3], Hongzhan Fei[2,e], Nico Giordano[4], Tomoo Katsura[2] & Hauke Marquardt[1]

[1]Department of Earth Sciences, University of Oxford, South Parks Road, OX1 3AN Oxford, United Kingdom.

[2]Bayerisches Geoinstitut, Universität Bayreuth, 95440 Bayreuth, Germany

[3]Department of Materials, University of Oxford, Parks Road, OX1 3PH Oxford, United Kingdom.

[4]Deutsches Elektronen-Synchrotron DESY, Notkestr. 85, 22607 Hamburg, Germany.

Abstract

Earth's lower mantle consists predominantly of two minerals, bridgmanite and Fe-bearing periclase, forming polycrystalline aggregates. Interpretation of seismic observations to constrain mantle temperature and composition requires a detailed understanding of the elastic behavior of mantle rocks. While the elastic properties of single-phase bridgmanite and periclase have been

[a]Present address: The Njord Centre, Department of Physics, University of Oslo, 0371 Oslo, Norway

[b]Present address: Diamond Light Source Ltd, Harwell Science and Innovation Campus, OX11 0DE Didcot, United Kingdom.

[c]Present address: Department of Earth and Environmental Sciences, Michigan State University, East Lansing, Michigan 48824, U.S.A.

[d]Present address: Institut für Mineralogie, Universität Münster, 48149 Münster, Germany.

[e]Present address: School of Earth Sciences, Zhejiang University, Hangzhou 310058, China

studied extensively, the bulk elastic properties of multiphase materials depend on how stress and strain are partitioned between the constituent phases, a process poorly understood.

Here, we present high-pressure synchrotron X-ray diffraction data on a sintered polycrystal of bridgmanite and periclase with estimated volume proportions of 7:3 and a bulk composition of $(Mg_{0.91}Fe_{0.09})_2SiO_4$, approximating a lower-mantle rock. We compare the compression behavior of the two-phase assemblage in quasi-hydrostatic conditions with and without high-temperature stress annealing. We find that bridgmanite forms a load-bearing framework, partially shielding periclase from the external confining pressure. During compression without annealing, this results in the development of under-pressure in the more compressible periclase. Consequently, the pressure-volume curve appears shallower relative to single-phase periclase and the onset of the iron spin crossover is suppressed, occurring at about 8 GPa higher external pressure. In contrast, when the two-phase assemblage is heated at 1800 K for around 1 minute, stresses are relaxed through plastic deformation and pressure is homogenized, producing compression curves consistent with single-phase measurements.

Our results indicate that stress-strain partitioning in multiphase materials is highly temperature-dependent, with compression behavior moving from a regime close to the iso-strain bound towards the iso-stress bound with increasing temperature. The relative timescales of pressure variations and stress-relaxation likely determine the bulk elastic behavior of a multiphase mantle rock when a seismic wave passes. Future experimental investigations of the temperature- and frequency-dependence of stress-strain partitioning in bridgmanite-periclase aggregates are key to accurately model seismic properties of lower-mantle rocks.

Keywords: bridgmanite, periclase, stress-strain partitioning, compression behaviour, lower mantle, iron spin crossover, multiphase material

Introduction

Knowledge of the elastic properties of the materials constituting Earth's deep interior is essential for seismic inversions (e.g., Buchen 2021; Marquardt and Thomson 2020), which can provide important information on the thermochemical structure of the mantle (e.g. Ballmer et al. 2017; Cobden et al. 2024; Davies et al. 2012; Deng et al. 2023; Gülcher et al. 2021; Mosca et al. 2012). The lower mantle consists predominantly of bridgmanite (~75 vol%) and a solid solution between periclase and wüstite (~18 vol%), which we shall refer to as periclase here-after (Irifune et al. 2010). High-pressure experiments and theoretical computations are used to determine the properties of these minerals at the extreme conditions of the deep Earth. Such studies typically focus on single-phase materials and the elastic properties of single crystals and powders of periclase and bridgmanite have been studied extensively (e.g. Boffa Ballaran et al. 2012; Catalli et al. 2010; Criniti et al. 2021; Kurnosov et al. 2017; Lin et al. 2005; Marquardt et al. 2009; Trautner et al. 2023; Wolf et al. 2015). However, the mantle is made of multiphase materials and the constituent minerals have different elastic properties (e.g. Irifune and Tsuchiya 2015; Stixrude and Lithgow-Bertelloni 2024), as well as plastic properties (e.g. Immoor et al. 2022). Understanding the relation between the properties of individual minerals and average elastic and rheological properties of a multiphase aggregate is key for the interpretation of seismic observations and modelling of geodynamic processes (Karato 2008).

The seismic wave velocities of multiphase materials are governed not only by volume fraction and the geometry of the constituent phases, but also by the stress-strain distribution (e.g., Watt et al. 1976). The Voigt (iso-strain) and Reuss (iso-stress) bounds represent two endmember models for the average elastic behavior of a multiphase aggregate (Karato 2008; Reuss 1929; Voigt 1928). The Voigt bound assumes that elastic strain is homogeneously distributed throughout the

material, so that the volume of each crystal in the aggregate changes by the same fraction upon compression. For a multiphase aggregate, with contrasting elastic properties of the constituent minerals, homogeneous strain will therefore result in a heterogeneous stress distribution. The Reuss bound, on the other hand, assumes that the imposed external stress field is homogeneous throughout a material. In this case, the stress state of each crystal in the aggregate will be the same, but the amount of strain will vary between phases. Sound wave velocities of lower mantle materials can be estimated by calculating the Voigt and Reuss bounds, but the resulting velocity variations can be several percent (Buchen 2021; Marquardt and Thomson 2020). While not based on any physical laws, the arithmetic mean of the bounds (Voigt-Reuss-Hill average) (Hill 1952) is most frequently used to approximate the elastic behavior of a polymineralic rock. In addition, stress-strain partitioning may well vary with temperature and the frequency of seismic waves. Thus, current knowledge of how stress and strain partition in mantle materials is limited, despite its importance for the interpretation of seismic observations. Complex compression behaviors of multiphase assemblages have been observed in high-pressure experiments (Glazyrin et al. 2016) and to improve mineral physics models for the seismic properties of mantle rocks, a better understanding of the processes governing the elastic response of multiphase materials is needed (Buchen 2021).

Here, we present compression data of a sintered polycrystalline aggregate of Fe-bearing bridgmanite and periclase, approximating a lower-mantle rock. We investigate how the compression behavior of the two-phase assemblage differs between experiments in quasi-hydrostatic conditions with and without high-temperature stress-annealing. We explain our observations by considering how stress and strain are partitioned between periclase and bridgmanite and we show how this affects the iron spin crossover in periclase (e.g., Badro et al.

2003; Lin et al. 2013). Finally, we consider the implications of our findings for future experimental studies on stress-strain partitioning in multi-phase materials and for estimating the bulk seismic properties of mantle materials.

Materials & Methods

Preparation of sample materials and diamond-anvil cells

Compression experiments in diamond-anvil cells (DACs) were performed on sintered aggregates of bridgmanite and periclase with sub-micron grain sizes. The detailed synthesis procedure is described in Fei et al. (2021) and can be summarized as follows: a sintered two-phase aggregate of bridgmanite and periclase was synthesized in a multi-anvil press at 27 GPa and 1700 K for 5 minutes. San Carlos olivine powder with an approximate composition of $(Mg_{0.91}Fe_{0.09})_2SiO_4$ was used as starting material, which should produce bridgmanite and periclase in a molar ratio of 1:1 (i.e. $(Mg,Fe)_2SiO_4 \rightarrow (Mg,Fe)SiO_3 + (Mg,Fe)O$), corresponding to an expected volume ratio of approximately 7:3. The synthesized polycrystal was polished to a thickness of approximately 10 μm and broken into pieces with diameters of <40 μm.

Two DACs with 200 μm culet size diamonds were prepared by pre-indenting rhenium gaskets to a thickness of ~30 μm and drilling a circular hole of ~90 μm in diameter using the laser cutting machine at the Department of Earth Sciences, University of Oxford. One cell (RT1) was prepared for compression at room-temperature in quasi-hydrostatic conditions: a piece of two-phase sample and a small piece of platinum foil, serving as pressure marker, were loaded in the centre of the diamond culet, before loading helium as a pressure-transmitting medium (PTM) using the gas-loading setup at beamline P02.2 at PETRA III, DESY, Germany (Liermann et al. 2015). After gas-loading, the pressure in the cell was ~8 GPa and the sample chamber had shrunk to a diameter of ~50 μm. Nevertheless, the sample remained isolated from the gasket

(supplemental figure S1a), and quasi-hydrostatic conditions were likely maintained throughout the experiment.

The second cell (LH1) was prepared for stress-annealing at high temperature by laser-heating. A piece of platinum foil was placed as pressure marker on one of the diamond culets, before a piece of sample, sandwiched between two layers of KCl of ~10 μm thickness, was loaded in the gasket hole (supplemental figure S1b). KCl served as both PTM and thermal insulation during laser-heating.

High-pressure experiments and sample characterization

The cells were compressed using a gas-membrane system at beamline P02.2, DESY. X-ray diffraction (XRD) images were collected in axial geometry on a Perkin-Elmer XRD1621 detector (Liermann et al. 2015), with a sample-detector distance of 412.1 mm. Tilting and rotation of the detector and sample-detector distance were calibrated using a CeO_2 standard (NIST 674b). Intense monochromatic synchrotron X-rays with a fixed wavelength of 0.2906 Å and a beam cross section with a full width of ~2×2 μm^2 at half of the intensity maximum (FWHM) were used. The sample in cell LH1 was annealed at high temperatures using a double-sided on-axis laser-heating system with a Yb-fiber laser available at beamline P02.2, DESY (Konôpková et al. 2021). The hot spot on the sample had a FWHM of ~10 μm and heating from both sides ensured the sample was heated uniformly along the axis of the X-ray beam. Temperatures were monitored using pyrometry of the light emitted from the hot sample (Konôpková et al. 2021).

In diffraction patterns of the two-phase sample, peaks from face-centered cubic periclase (space group $Fm\bar{3}m$) partially overlap with the large number of diffraction peaks of orthorhombic bridgmanite (space group *Pbnm*) (fig. 1). To keep fitting of the diffraction patterns as

straightforward as possible, the pressure marker was placed next to the samples (supplemental figure S1). For each measurement of cell RT1, pressure was increased by ~2 GPa and left to stabilize for a few minutes. Then, a diffraction image of the pressure marker was recorded directly before and after taking a measurement of the sample. This resulted in a total of 47 XRD images of the sample in RT1 at pressures between 8 GPa and 86 GPa. During the 10 s exposure, the cell was rotated by ± 5° around the vertical axis (perpendicular to the X-ray beam). The images of the pressure marker had a 3 s exposure, without rotation.

Cell LH1 was pre-compressed to 28 GPa to prevent amorphization of bridgmanite during laser-heating. Pressure was increased in steps of ~2 GPa and the sample was annealed by laser-heating at each pressure step. Each time the pressure was increased, the cell was allowed to stabilize for a few minutes and the pressure marker was measured prior to recording an XRD image of the sample. The sample was then heated to ~1800 K at spot 1 (supplemental figure S1b) for around 1 minute to anneal stresses. After quenching to room temperature, the sample was measured again before taking another XRD image of the pressure marker. A total of 37 images were taken of the sample at pressures between 28 GPa and 74 GPa. The exposure time for images of the sample was 5 s for the first three pressure steps and was then increased to 10 s, to improve intensity of the diffraction peaks. The exposure time for images of the pressure marker was 3 s. After cell LH1 was compressed to 74 GPa, the sample was heated at ~2200 K at a different position (spot 2, supplemental figure S1b) for ~15 minutes, to investigate how prolonged heating at high temperature affects the sample.

To acquire zero-pressure volumes (V_0) of the two phases in the sintered sample, a piece of sample was placed on top of a diamond culet and a diffraction pattern was measured in air at ambient pressure and temperature at beamline P02.2, DESY. The exposure time for this

157 measurement was 1 s, and the X-rays had a wavelength of 0.4845 Å, with a beam size of 3×8
158 μm^2 (FWHM).

159 After the compression experiment, the sample from cell LH1 was recovered and any remaining
160 KCl was removed by dissolution in de-ionised water. The sample was mounted on a holder and
161 analysed using a ThermoFisher Helios G4CXe Xenon Plasma FIB/SEM system (Focussed Ion
162 Beam/Scanning Electron Microscope), equipped with an Oxford Instruments UltimMax 170 X-
163 ray detector for Energy Dispersive X-ray Spectroscopy (EDS), at the David Cockayne Centre for
164 Electron Microscopy, Department of Materials, University of Oxford, UK. The FIB was used to
165 cut and polish cross sections parallel to the compression axis across both laser-heating spots.
166 Cross sections were imaged with the SEM, and EDS measurements were taken to map elemental
167 distribution (fig. 2), processed using Oxford Instruments Aztec software. During imaging, the
168 sample was tilted by 52°, with a working distance of 3.9 mm. An acceleration voltage of 5 kV
169 and processing time of 6 s were used. The EDS map of spot 1 (fig. 2b) was collected with a 2733
170 s livetime, yielding ~43 million counts and the map of spot 2 (fig. 2a) was collected with a 1733
171 s livetime, yielding ~26 million counts.

172 **Diffraction data processing and pressure determination**

173 The program Dioptas (Prescher and Prakapenka 2015) was used to integrate the collected
174 diffraction images. The lattice parameters of bridgmanite, periclase and platinum, and the
175 corresponding uncertainties, were extracted from the diffraction patterns by LeBail refinement
176 with GSAS-II (Toby and Von Dreele 2013). Representative fitted diffraction patterns of the
177 sample for different experimental conditions are shown in figure 1. Platinum was fitted with a
178 face-centred cubic crystal structure (space group $Fm\bar{3}m$). Parasitic peaks of rhenium (fitted with
179 a hexagonal close-packed crystal structure, space group $P6_3/mmc$) could not be avoided in the

180 experimental run in helium, because of the shrinkage of the sample chamber. Peaks of KCl
181 (fitted with a body-centred cubic structure, space group $Pm\bar{3}m$) are present in the patterns from
182 cell LH1.

183 The unit-cell volume of platinum was used to determine the pressure for all data sets, employing
184 previously published third-order Birch-Murnaghan Equation of State (EoS) parameters (Fei et al.
185 2007). Pressure in cell RT1 at each pressure step was determined from the arithmetic average of
186 the pressures recorded before and after measurement of the sample, while pressure of the sample
187 in cell LH1 was derived from the pressure measurement closest in time to the sample
188 measurement (i.e., before or after heating). For both cells, uncertainty in pressure was estimated
189 from the difference between the two pressure measurements at each step and the uncertainty of
190 the measurements themselves, propagated from the uncertainty in the unit-cell volumes of
191 platinum. The time delay between measurements of the sample and the pressure standard
192 introduced additional uncertainty to the estimated pressure of the sample. However, by letting
193 the pressure stabilize between pressure steps and measuring the pressure standard directly
194 before/after the sample this uncertainty was minimized. This is supported by the small difference
195 in the pressures measured before and after the measurement on the sample (i.e., 0.3 GPa in RT1
196 and 0.5 GPa in LH1 on average). The physical separation between the pressure standard and the
197 sample may produce a further small systematic pressure error if pressure gradients were present
198 in the sample chamber, although this should be minimized in RT1 and LH1 by the quasi-
199 hydrostaticity of helium and high-temperature stress annealing, respectively. We note that the
200 simultaneous measurement of the volumes of bridgmanite and periclase in the two-phase sample
201 allows for direct comparison of their relative compression behaviors irrespective of the absolute
202 pressure scale.

Results & Discussion

Microstructure and composition of the bridgmanite-periclase polycrystal

Periclase and bridgmanite grains can be distinguished by brightness in backscattered electron (BSE) images of the laser-heated sample recovered from cell LH1, with bridgmanite appearing darker (fig. 2, top row). The distribution of both phases is homogeneous in unheated areas, with grain sizes varying from about 0.1 μm to 0.5 μm. The two phases are also discernible in EDS elemental maps of Si and Mg, with a strong Si signal indicating bridgmanite and a strong Mg signal corresponding to periclase grains (fig. 2). The expected volume ratio of bridgmanite to periclase based on the olivine starting material (i.e., 7:3) is in good agreement with visual estimates from the back-scattered electron images (fig. 2), as well as with a volume ratio of 73:27 produced by fitting of the diffraction pattern collected at 0 GPa. Whilst the distribution of Fe appears mostly homogeneous in unheated areas of the sample, we observe one region enriched in Fe, as well as a comparatively high Al-concentration of around 1.5 at.% (of all atoms). This suggests the presence of some impurities or contamination in the starting material and implies that the bulk composition of the sample can deviate locally from $(Mg_{0.91}Fe_{0.09})_2SiO_4$.

The grain size of the sample is too small to measure the composition of individual crystals by EDS, but the spectra can nonetheless provide some information on bulk iron content and iron distribution. In spot 1, where the compression data were collected, we find an average iron number (i.e. Fe/[Fe+Mg]) of $Fe\# = 0.063$, which is lower than expected from the theoretical bulk composition (i.e., $Fe\# = 0.09$). However, measurements of composition with EDS are not very precise; the standard-less analysis method employed here has a relative deviation from the expected value of ± 25% (Goldstein et al. 2018). To constrain the iron distribution between bridgmanite and periclase, we have derived spectra of comparatively Si-rich and Si-poor regions,

This is the peer-reviewed, final accepted version for American Mineralogist, published by the Mineralogical Society of America.
The published version is subject to change. Cite as Authors (Year) Title. American Mineralogist, in press.
DOI: https://doi.org/10.2138/am-2025-10040. http://www.minsocam.org/

which correspond to bridgmanite-rich and periclase-rich material, respectively (supplemental figure S2). We can use the Si content as a proxy for the relative proportions of the two phases in the measured region. The measured *Fe#* as a function of silicon number (i.e., Si at.% normalized with respect to the total cation content, or Si/[Fe+Mg+Si]) falls on a mixing line between the x_{Fe} of periclase (at 0 Si#) and x_{Fe} of bridgmanite (at 0.5 Si#) (supplemental figure S3). We find that *Fe#* in the bridgmanite-rich areas is higher than in the periclase-rich areas, suggesting a partition coefficient $K_D < 1$, where $K_D = [Fe/Mg]_{Per}/[Fe/Mg]_{Bg}$.

The zero-pressure volumes of the two phases, measured by XRD (figs. 1a and 3), provide additional constraints on iron distribution. For $(Mg_{1-x}Fe_x)O$ periclase, we found $V_0 = 75.269(3)$ Å^3, suggesting $x_{Fe} \approx 0.085$ (Jacobsen et al. 2002; Trautner et al. 2024). Bridgmanite in the two-phase mixture has $V_0 = 164.446(5)$ Å^3. While iron in periclase is expected to be predominantly ferrous for low iron contents (McCammon et al. 1998), iron in bridgmanite can exist as both Fe^{2+} and Fe^{3+} and is able to occupy both the dodecahedral and octahedral sites. Fe^{3+} expands the unit-cell volume of bridgmanite more than Fe^{2+} relative to the Mg-endmember (Catalli et al. 2010). The V_0 of bridgmanite in our sample indicates a minimum iron content of ~0.11 per three oxygen per formula unit if the $Fe^{3+}/\Sigma Fe$ is high (Hummer and Fei 2012). The iron contents of bridgmanite and periclase estimated from the measured V_0 then indicate $K_D \leq 0.8$, which is consistent with the EDS measurements.

It is well-known that laser-heating of iron-bearing samples in DACs can lead to Soret diffusion, i.e., chemical diffusion driven by a temperature gradient (e.g. Sinmyo and Hirose 2010). Since changes in composition often lead to changes in the unit-cell volume of minerals, chemical segregation in the laser-heating spot could distort the compression data collected after laser-annealing in cell LH1. To ensure that the collected data represent compression curves for

constant composition of both minerals, we compare BSE images and EDS elemental maps of the cross sections of spot 1, where the data was collected after repeatedly heating for short periods at 1800 K, and of spot 2, which was heated for ~15 minutes at 2200 K (fig. 2). In spot 2, we find clear signs of chemical segregation, as well as changes in the volume fractions and compositions of mineral phases. The sample has recrystallized with large (~1.5 μm) iron-depleted bridgmanite grains forming in the centre and iron-enriched periclase concentrated in a rim surrounding the hotspot (see also supplemental figure S4c). Migration of iron away from the hot center is in good agreement with the observations of Sinmyo and Hirose (2010). None of the effects of laser-heating in spot 2 are observed in spot 1: grain size and volume fractions of periclase and bridgmanite remain unchanged and no variations in iron concentration are observed (fig. 2b), nor do the XRD images show signs of recrystallization (supplemental figure S4b). From this we conclude that the laser-annealing in spot 1 did not cause chemical segregation, likely because of the lower temperature than in spot 2.

Compression curves of periclase and bridgmanite in a two-phase mixture

The pressure-volume (*P*-*V*) measurements for periclase in the sintered two-phase aggregate with and without stress-annealing are shown in figure 3a. The compression curve of periclase from the annealed sample is in excellent agreement with previously published compression data for powders of $(Mg_{0.9}Fe_{0.1})O$ (Marquardt et al. 2009) and $(Mg_{0.83}Fe_{0.17})O$ (Lin et al. 2005), as well as the $P(V)$-curve of $(Mg_{0.81}Fe_{0.19})O$ predicted by *ab initio* computations (Trautner et al. 2023). In contrast, we observe a striking difference in compression behavior in the sample without annealing: the compression curve is much shallower, i.e., shifted to increasingly higher volumes with increasing pressure, compared to the annealed data. This cannot be attributed to

271 compositional differences, since EDS analysis showed no evidence of Soret diffusion as
272 discussed in the previous section.

273 The $P(V)$ data for bridgmanite in the annealed and unannealed two-phase sample are shown in
274 figure 3b, together with literature results for single-crystal $(Mg_{0.96}Fe_{0.04})SiO_3$ (Boffa Ballaran et
275 al. 2012) and powder of $(Mg_{1-x}Fe_x)(Si_{1-x}Fe_x)O_3$ with $x_{Fe} = 0.1$ (Catalli et al. 2010). The lattice
276 parameters as a function of pressure are shown in supplemental figure S5. The volumes for
277 bridgmanite in the unannealed sample are in good agreement with literature data, showing no
278 signs of a deviation from the previously reported compression behavior, as observed for periclase
279 in the unannealed two-phase sample. A slight offset in the volume curves is likely due to
280 differences in iron content and oxidation state, since the unit-cell volume of bridgmanite is
281 known to increase with both $Fe^{3+}/\Sigma Fe$ and total iron content (Boffa Ballaran et al. 2012; Catalli
282 et al. 2010). The trend of the compression curve for bridgmanite in the annealed sample is also
283 consistent with the literature data, but it is shifted to higher volumes relative to the unannealed
284 sample with a near-constant offset. This observed offset might result from systematic errors in
285 the here-determined volumes of bridgmanite in the annealed sample that were complicated by
286 peak overlap with KCl and periclase, making it difficult to constrain the three unique lattice
287 parameters of orthorhombic bridgmanite (fig. 1c). However, heating the sample might also have
288 caused an increase in $Fe^{3+}/\Sigma Fe$, which is known to expand the unit-cell volume (Catalli et al.
289 2010). In addition, the offset from previous studies may also be the result of errors in the
290 pressure determination caused by differences in the pressure markers and scales used.

291 Glazyrin et al. (2016) have previously studied the compression of a bridgmanite-periclase
292 mixture with a Fe-, Al-, Ca-bearing mantle-like composition, comparing results from
293 experiments with an unannealed sample under strongly non-hydrostatic conditions to an

294 annealed sample surrounded by a pressure medium. Before laser-annealing they observed
295 anomalous compression behavior not just in periclase, but also in bridgmanite, which contrasts
296 with our observations for the unannealed two-phase sample. We can explain this by the
297 differences in hydrostaticity of the experiments: the sample studied by Glazyrin et al. (2016) was
298 bridging the walls of the sample chamber, producing a strong deviatoric stress component, while
299 our sample in cell RT1 was completely surrounded by helium and thus under quasi-hydrostatic
300 conditions. Nonetheless, we find that the volume of periclase in the unannealed sample is ~3.5%
301 larger than expected from single-phase measurements at 80 GPa, suggesting that the stress-state
302 inside the sintered two-phase aggregate differs from the external quasi-hydrostatic pressure
303 acting on the polycrystal. We attribute this to stress-strain partitioning effects between
304 bridgmanite and periclase, as discussed in the following section.

305 **Stress-strain partitioning between periclase and bridgmanite**

306 The bulk elastic behavior of the two-phase sample is expected to lie between the Voigt and
307 Reuss bounds, i.e. homogeneous strain or homogeneous stress, respectively (Karato 2008; Reuss
308 1929; Voigt 1928). Differences in how stress and strain are partitioned between periclase and
309 bridgmanite may explain the contrasting compression behavior of periclase in our experiments
310 with and without laser-annealing. The use of a soft pressure-transmitting medium in a DAC
311 experiment ensures that deviatoric stress in the sample chamber is minimal and that the sample
312 as a whole experiences quasi-hydrostatic compression. However, even if the bulk macroscopic
313 stress is hydrostatic, anisotropy and differences in the compressibility of the constituent phases
314 of a sintered polycrystalline and/or multiphase material will result in deviatoric stresses
315 developing within grains and at the grain boundaries (e.g., Angel et al. 2015; Buchen et al. 2018;

316 Wang et al. 2023). Whether these stresses are accommodated elastically or plastically depends
317 on whether they exceed the material's yield strength.

318 Bridgmanite is generally thought to be plastically stronger than periclase at experimental strain
319 rates (Girard et al. 2016; Immoor et al. 2022; Miyagi and Wenk 2016), although this may reverse
320 at the low strain rates naturally occurring in the mantle (Cordier et al. 2023). The volume
321 proportions of bridgmanite and periclase in the two-phase sample are approximately 7:3 and
322 back-scattered electron images of the sample (fig. 2) show that periclase grains are not
323 interconnected (at least not in the two-dimensional cross-section sampled). This suggests that
324 bridgmanite, as the stronger and volumetrically dominant phase, forms a load-bearing framework
325 (Handy 1994), imposing its strain on periclase by shielding periclase grains from the external
326 stress field up to the yield strength of the bridgmanite grains.

327 The anomalous compression behavior of periclase in the two-phase sample without laser
328 annealing can thus be explained by elastic deformation close to the iso-strain bound. Because
329 bridgmanite is less compressible than periclase (e.g., Boffa Ballaran et al. 2012; Marquardt et al.
330 2009), the pressure transmitted to periclase by elastic deformation of the bridgmanite framework
331 is lower than the external confining pressure, resulting in a less steep compression curve. In
332 contrast, the compression behavior of the two-phase sample with laser-annealing appears close to
333 the iso-stress bound: periclase in the two-phase sample exhibits the same compression behavior
334 after laser-annealing as single-phase periclase in previous sudies (fig. 3a), indicating that the
335 pressure acting on the periclase grains is equal to the external confining pressure. This is
336 illustrated schematically in figure 4. Laser-annealing homogenizes stresses in the sample,
337 because the yield strength of bridgmanite is reduced at higher temperatures and deviatoric
338 stresses are relaxed through plastic deformation (Glazyrin et al. 2016; Kraych et al. 2016). In

This is the peer-reviewed, final accepted version for American Mineralogist, published by the Mineralogical Society of America.
The published version is subject to change. Cite as Authors (Year) Title. American Mineralogist, in press.
DOI: https://doi.org/10.2138/am-2025-10040. http://www.minsocam.org/

addition, an increase in the $Fe^{3+}/\Sigma Fe$ of bridgmanite during laser-heating might also contribute to homogenization of stresses by increasing the number of oxygen vacancies and decreasing creep strength (Fei et al. 2021).

We can further investigate the stress-strain partitioning in the sample by looking at normalized volume strain ($\varepsilon = [V\text{-}V_{ref}]/V_{ref}$) as a function of pressure (fig. 5). Since the two-phase sample was synthesized at 27 GPa (Fei et al. 2021) and decompression to room pressure is likely to have changed the stress state, we use the volumes that were determined for each phase at 27 GPa as V_{ref}. We compare our results for the sintered two-phase aggregate with single-phase data on Fe-bearing periclase and bridgmanite from literature (Boffa Ballaran et al. 2012; Catalli et al. 2010; Lin et al. 2005; Marquardt et al. 2009). We find that the derivative of the strain-pressure curve in single-phase periclase is larger than for single-phase bridgmanite (fig. 5), as expected from the higher compressibility of periclase (e.g. Boffa Ballaran et al. 2012; Marquardt et al. 2009). For the annealed sample, the strain of both phases is in excellent agreement with the single-phase data, confirming that the elastic behavior of the sample in this experiment is best described by the iso-stress model. For the unannealed sample, the strain of bridgmanite is also consistent with the single-phase data. However, the strain of periclase is intermediate between that of single-phase periclase and that of bridgmanite, suggesting that stress-strain partitioning in the unannealed sample is intermediate between the Voigt and Reuss bounds.

The pressure difference between periclase in the annealed and unannealed sample for the same strain may be related to the yield stress of bridgmanite, i.e., the maximum shear stress that can be supported before plastic deformation occurs and the confining pressure is partially transmitted to periclase. Between ε=0 (i.e., at 27 GPa) and ε=-0.1, the pressure difference between the pressure-strain curves of annealed and unannealed periclase in the two-phase sample increases from ~0

GPa to ~8 GPa (fig. 5 and supplemental figure S6). This is approximately half of the yield strength observed in bridgmanite at room temperature and high pressure (Miyagi 2021). We note that the yield strength will be lattice-plane dependent, i.e., anisotropic, and related to the critical resolved shear stress (e.g., Kraych et al. 2016; Lin et al. 2017). It is thus expected that some plastic flow occurs at stresses below the bulk yield strength.

Effects of stress-strain partitioning on the iron spin crossover in periclase

At high pressure, ferrous iron in Fe-bearing periclase undergoes an electronic reconfiguration from high-spin to low-spin state (e.g., Badro et al. 2003; Lin et al. 2013). This spin crossover is associated with an enhanced reduction in unit-cell volume of periclase and softening of the bulk modulus, which is thought to lead to changes in seismic velocities of the lower mantle (e.g. Cobden et al. 2024; Crowhurst et al. 2008; Marquardt et al. 2018; Marquardt et al. 2009; Méndez et al. 2022; Trautner et al. 2023; Wu et al. 2013). The partitioning of stress and strain between bridgmanite and periclase in the two-phase aggregate is likely to affect the spin state of iron in periclase, since the spin crossover is sensitive to the iron-oxygen bond length, which changes with pressure (Badro 2014; Lin et al. 2013).

The iron spin crossover-induced volume reduction occurs gradually, making it difficult to pinpoint the onset pressure in the *P(V)*-curve of periclase (fig. 3a). It is more easily identified in a plot of normalized stress F as a function of pressure, where $F = \frac{P}{3f(1+2f)^{5/2}}$ and Eulerian strain $f = 0.5\,(\frac{V_0^{\frac{2}{3}}}{V} - 1)$ (Angel 2000; Stacey et al. 1981). Therefore, we calculate the normalized stress of periclase in our experiments. We use the measured zero-pressure volume for periclase in the two-phase aggregate for the data collected without laser-annealing. For the data on the annealed

sample we use the V_0 reported by Marquardt et al. (2009), because it is in better agreement with the extrapolated pressure-strain curve (fig. 5).

In the *F-P* plot (fig. 6), the spin crossover in Fe-bearing periclase is marked by a drop in normalized stress (e.g. Glazyrin et al. 2016; Solomatova et al. 2016). We find that the spin crossover in periclase in the two-phase sample occurs between approximately 40-60 GPa with laser-annealing and between about 48-72 GPa without laser-annealing. Note that these pressures represent the external quasi-hydrostatic pressure determined from platinum and do not necessarily correspond to the pressure experienced by periclase inside the sample. The apparent shift of the onset to higher pressure and broadening of the spin crossover range in the unannealed sample is consistent with periclase experiencing a lower confining pressure than expected from the external pressure in the sample chamber, because it is shielded by less compressible bridgmanite.

The intercept on the *F* axis of the *F-P* plot corresponds to the value of the bulk modulus at ambient conditions (K_0). Single-phase periclase has a K_0 around 158 GPa (Marquardt et al. 2009), while single-phase bridgmanite has a K_0 around 250 GPa (Boffa Ballaran et al. 2012). Despite the large scatter in the *F-P* plot at low pressures typical for such plots (Angel 2000), it is evident that K_0 of periclase for the unannealed sample (about 180 GPa, fig. 6) appears intermediate between the values of single-phase periclase and bridgmanite. This is further evidence suggesting that, at ambient temperature, the elastic behavior of periclase in the two-phase aggregate is controlled by the compressibility and yield strength of bridgmanite.

Implications

Our experimental investigation of the compression behavior of a sintered two-phase aggregate of Fe-bearing bridgmanite and periclase under quasi-hydrostatic conditions shows that a load-

406 bearing framework of bridgmanite can partially shield periclase from the external confining
407 pressure, affecting the spin state of iron in periclase. The phenomenon of over- or under-pressure
408 development in isolated grains within a multi-phase system as a result of differences in
409 thermoelastic properties of the phases is well-known in host-inclusion systems (Angel et al.
410 2015). For example, the residual over-pressure in silicate inclusions in natural diamonds after
411 they have been transported to the surface can be used to constrain the conditions of entrapment
412 (e.g.Howell et al. 2012; Nestola et al. 2011), i.e., elastic barometry. Moreover, the development
413 of under-pressure in quartz inclusions in garnet during subduction can prevent a transition to
414 coesite, even if external pressure-temperature conditions have reached the coesite stability field
415 (Alvaro et al. 2019). This is comparable to the suppression of the spin crossover in the
416 unannealed two-phase sample observed in our experiments. Whether or not such pressures
417 differences in confined phases are preserved depends on the strength of the host phase, as well as
418 the timescales of stress-relaxation through plastic deformation.

419 We have shown that the compression behaviour of the sintered bridgmanite-periclase aggregate
420 is closer to the iso-strain bound in quasi-hydrostatic conditions without laser-annealing, but
421 changes to iso-stress with annealing. This implies that stress-strain partitioning between
422 bridgmanite and periclase is sensitive to temperature, shifting towards the Reuss bound with
423 increasing temperatures as the yield strength of bridgmanite decreases. In addition to a
424 temperature-dependence of stress-strain partitioning, it may be expected that there also is a time-
425 dependence, related to element diffusion rates that govern the plastic deformation mechanisms
426 allowing stresses to homogenize. This would open the possibility that the Reuss bound applies to
427 slow geologic processes at high temperatures, whereas the Voigt bound may be more relevant for
428 rapid seismic deformations.

We found that heating the two-phase sample to 1800 K for a relatively short period of time (i.e., around 1 minute) is sufficient to anneal stresses and equilibrate pressure in the sample, although the required time/temperature likely depends on grain size. Since temperatures in the lower mantle are thought to exceed 1800 K, we do not expect any pressure differences to develop in periclase and bridgmanite during upwelling or downwelling over geologic timescales. However, compressional seismic waves travelling through Earth's interior produce pressure variations over much shorter timescales, i.e., milliseconds to minutes. If a passing seismic wave produces pressure-differences within a multi-phase rock, this could affect the average elastic properties of the rock in a dynamic way and would have to be considered in the interpretation of seismic observations. In particular, for lower mantle rocks consisting primarily of bridgmanite and Fe-bearing periclase, the shielding effect of bridgmanite may impact the seismic signature of the iron spin crossover.

Improving our understanding of the temperature- and frequency-dependence of stress-strain partitioning is key to accurately model the elastic behavior of a polymineralic rock and interpret seismic observations (Buchen 2021). Experimental capabilities are advancing with the development of (radial) dynamic diamond anvil cells (Huston et al. 2024; Jenei et al. 2019; Marquardt et al. 2018; Méndez et al. 2020; Wang et al. 2026). These techniques can be used to perform cyclic loading experiments, opening up the potential for measuring stress-strain partitioning in polycrystalline materials at lower-mantle pressures and at the frequencies of seismic waves. Such measurements will allow future studies to improve mineral physics models for the seismic properties of lower-mantle rocks, in particular by further investigating how the complex elastic behavior of bridgmanite-periclase aggregates described in this study is affected by oscillating stresses.

Acknowledgments

This research received funding through the European Union's Horizon 2020 research and innovation programme (ERC Grant 864877 awarded to HM and ERC Grant 787527 awarded to TK). Beamline P02.2, PETRA III, DESY (Hamburg, Germany), a member of the Helmholtz Association HGF, is acknowledged for the provision of experimental facilities. The authors acknowledge use of characterisation facilities within the David Cockayne Centre for Electron Microscopy, Department of Materials, University of Oxford, alongside financial support provided by the Henry Royce Institute (Grant ref EP/R010145/1). For the purpose of Open Access, the authors have applied a CC BY public copyright licence to any Author Accepted Manuscript (AAM) version arising from this submission.

References

Alvaro, M., Mazzucchelli, M.L., Angel, R.J., Murri, M., Campomenosi, N., Scambelluri, M., Nestola, F., Korsakov, A., Tomilenko, A.A., Marone, F., and Morana, M. (2019) Fossil subduction recorded by quartz from the coesite stability field. Geology, 48(1), 24-28.

Angel, R.J. (2000) Equations of State. In R.M. Hazen, and R.T. Downs, Eds. High-temperature and high-pressure crystal chemistry, p. 35-60. The Mineralogical Society of America, Washington, DC.

Angel, R.J., Nimis, P., Mazzucchelli, M.L., Alvaro, M., and Nestola, F. (2015) How large are departures from lithostatic pressure? Constraints from host–inclusion elasticity. Journal of Metamorphic Geology, 33(8), 801-813.

Badro, J. (2014) Spin Transitions in Mantle Minerals. Annual Review of Earth and Planetary Sciences, 42(1), 231-248.

Badro, J., Fiquet, G., Guyot, F., Rueff, J.-P., Struzhkin, V.V., Vankó, G., and Monaco, G. (2003) Iron Partitioning in Earth's Mantle: Toward a Deep Lower Mantle Discontinuity. Science, 300(5620), 789-791.

Ballmer, M.D., Houser, C., Hernlund, J.W., Wentzcovitch, R.M., and Hirose, K. (2017) Persistence of strong silica-enriched domains in the Earth's lower mantle. Nature Geoscience, 10(3), 236-240.

Boffa Ballaran, T., Kurnosov, A., Glazyrin, K., Frost, D.J., Merlini, M., Hanfland, M., and Caracas, R. (2012) Effect of chemistry on the compressibility of silicate perovskite in the lower mantle. Earth and planetary science letters, 333-334, 181-190.

Buchen, J. (2021) Seismic Wave Velocities in Earth's Mantle from Mineral Elasticity. In H. Marquardt, M.D. Ballmer, S. Cottaar, and J. Konter, Eds. Mantle Convection and Surface Expressions, p. 51-95. American Geophysical Union, Washington, DC.

Buchen, J., Marquardt, H., Schulze, K., Speziale, S., Boffa Ballaran, T., Nishiyama, N., and Hanfland, M. (2018) Equation of State of Polycrystalline Stishovite Across the Tetragonal-Orthorhombic Phase Transition. Journal of Geophysical Research: Solid Earth, 123(9), 7347-7360.

Catalli, K., Shim, S.-H., Prakapenka, V.B., Zhao, J., Sturhahn, W., Chow, P., Xiao, Y., Liu, H., Cynn, H., and Evans, W.J. (2010) Spin state of ferric iron in $MgSiO_3$ perovskite and its effect on elastic properties. Earth and Planetary Science Letters, 289(1-2), 68-75.

Cobden, L., Zhuang, J., Lei, W., Wentzcovitch, R., Trampert, J., and Tromp, J. (2024) Full-waveform tomography reveals iron spin crossover in Earth's lower mantle. Nature Communications, 15(1).

Cordier, P., Gouriet, K., Weidner, T., Van Orman, J., Castelnau, O., Jackson, J.M., and Carrez, P. (2023) Periclase deforms more slowly than bridgmanite under mantle conditions. Nature, 613(7943), 303-307.

Criniti, G., Kurnosov, A., Boffa Ballaran, T., and Frost, D.J. (2021) Single-Crystal Elasticity of $MgSiO_3$ Bridgmanite to Mid-Lower Mantle Pressure. Journal of Geophysical Research: Solid Earth, 126(5), e2020JB020967.

Crowhurst, J.C., Brown, J.M., Goncharov, A.F., and Jacobsen, S.D. (2008) Elasticity of (Mg,Fe)O Through the Spin Transition of Iron in the Lower Mantle. Science, 319(5862), 451-453.

Davies, D.R., Goes, S., Davies, J.H., Schuberth, B.S.A., Bunge, H.P., and Ritsema, J. (2012) Reconciling dynamic and seismic models of Earth's lower mantle: The dominant role of thermal heterogeneity. Earth and planetary science letters, 353-354, 253-269.

Deng, X., Xu, Y., Hao, S., Ruan, Y., Zhao, Y., Wang, W., Ni, S., and Wu, Z. (2023) Compositional and thermal state of the lower mantle from joint 3D inversion with seismic tomography and mineral elasticity. Proceedings of the National Academy of Sciences, 120(26), e2220178120.

Fei, H., Faul, U., and Katsura, T. (2021) The grain growth kinetics of bridgmanite at the topmost lower mantle. Earth and Planetary Science Letters, 561, 116820.

Fei, Y., Ricolleau, A., Frank, M., Mibe, K., Shen, G., and Prakapenka, V. (2007) Toward an internally consistent pressure scale. Proceedings of the National Academy of Sciences, 104(22), 9182-6.

517 Girard, J., Amulele, G., Farla, R., Mohiuddin, A., and Karato, S.-i. (2016) Shear deformation of
518 bridgmanite and magnesiowüstite aggregates at lower mantle conditions. Science,
519 351(6269), 144-147.
520 Glazyrin, K., Miyajima, N., Smith, J.S., and Lee, K.K.M. (2016) Compression of a multiphase
521 mantle assemblage: Effects of undesirable stress and stress annealing on the iron spin
522 state crossover in ferropericlase. Journal of Geophysical Research: Solid Earth, 121(5),
523 3377-3392.
524 Goldstein, J.I., Newbury, D.E., Michael, J.R., Ritchie, N.W.M., Scott, J.H.J., and Joy, D.C.
525 (2018) Scanning Electron Microscopy and X-Ray Microanalysis. Springer New York,
526 New York, NY.
527 Gülcher, A.J.P., Ballmer, M.D., and Tackley, P.J. (2021) Coupled dynamics and evolution of
528 primordial and recycled heterogeneity in Earth's lower mantle. Solid Earth, 12(9), 2087-
529 2107.
530 Handy, M.R. (1994) Flow laws for rocks containing two non-linear viscous phases: A
531 phenomenological approach. Journal of structural geology, 16(3), 287-301.
532 Hill, R. (1952) The Elastic Behaviour of a Crystalline Aggregate. Proceedings of the Physical
533 Society. Section A, 65(5), 349-354.
534 Howell, D., Wood, I.G., Nestola, F., Nimis, P., and Nasdala, L. (2012) Inclusions under remnant
535 pressure in diamond; a multi-technique approach. An international journal of Mineralogy,
536 Petrology, Geochemistry and related sciences, 24(4), 563-573.
537 Hummer, D.R., and Fei, Y. (2012) Synthesis and crystal chemistry of Fe3+-bearing
538 (Mg,Fe3+)(Si,Fe3+)O3 perovskite. The American mineralogist., 97(11-12), 1915-1921.

539 Huston, L.Q., Miyagi, L., Husband, R.J., Glazyrin, K., Kiessner, C., Wendt, M., Liermann, H.P.,
540 and Sturtevant, B.T. (2024) New dynamic diamond anvil cell for time-resolved radial x-
541 ray diffraction. Review of Scientific Instruments, 95(4).
542 Immoor, J., Miyagi, L., Liermann, H.-P., Speziale, S., Schulze, K., Buchen, J., Kurnosov, A., and
543 Marquardt, H. (2022) Weak cubic $CaSiO_3$ perovskite in the Earth's mantle. Nature,
544 603(7900), 276-279.
545 Irifune, T., Shinmei, T., McCammon, C.A., Miyajima, N., Rubie, D.C., and Frost, D.J. (2010)
546 Iron Partitioning and Density Changes of Pyrolite in Earth's Lower Mantle. Science,
547 327(5962), 193-195.
548 Irifune, T., and Tsuchiya, T. (2015) 2.03 - Phase Transitions and Mineralogy of the Lower
549 Mantle. In G. Schubert, Ed. Treatise on Geophysics, 2, p. 33-60. Elsevier B.V.
550 Jacobsen, S.D., Reichmann, H.-J., Spetzler, H.A., Mackwell, S.J., Smyth, J.R., Angel, R.J., and
551 McCammon, C.A. (2002) Structure and elasticity of single-crystal (Mg,Fe)O and a new
552 method of generating shear waves for gigahertz ultrasonic interferometry. Journal of
553 Geophysical Research, 107(B2), ECV 4-1 - ECV 4-14.
554 Jenei, Z., Liermann, H.P., Husband, R., Mendez, A.S.J., Pennicard, D., Marquardt, H.,
555 O'Bannon, E.F., Pakhomova, A., Konopkova, Z., Glazyrin, K., Wendt, M., Wenz, S.,
556 McBride, E.E., Morgenroth, W., Winkler, B., Rothkirch, A., Hanfland, M., and Evans,
557 W.J. (2019) New dynamic diamond anvil cells for tera-pascal per second fast
558 compression x-ray diffraction experiments. Review of Scientific Instruments, 90, 065114.
559 Karato, S.-i. (2008) Deformation of earth materials: an introduction to the rheology of solid
560 earth. Cambridge University Press, Cambridge.

561 Konôpková, Z., Morgenroth, W., Husband, R., Giordano, N., Pakhomova, A., Gutowski, O.,
562 Wendt, M., Glazyrin, K., Ehnes, A., Delitz, J.T., Goncharov, A.F., Prakapenka, V.B., and
563 Liermann, H.-P. (2021) Laser heating system at the Extreme Conditions Beamline, P02.2,
564 PETRA III. Journal of Synchrotron Radiation, 28(6), 1747-1757.
565 Kraych, A., Carrez, P., and Cordier, P. (2016) On dislocation glide in MgSiO 3 bridgmanite at
566 high-pressure and high-temperature. Earth and planetary science letters, 452, 60-68.
567 Kurnosov, A., Marquardt, H., Frost, D.J., Boffa Ballaran, T., and Ziberna, L. (2017) Evidence
568 for a Fe^{3+}-rich pyrolitic lower mantle from (Al,Fe)-bearing bridgmanite elasticity data.
569 Nature, 543(7646), 543-546.
570 Liermann, H.-P., Konôpková, Z., Morgenroth, W., Glazyrin, K., Bednarčik, J., Mcbride, E.E.,
571 Petitgirard, S., Delitz, J.T., Wendt, M., Bican, Y., Ehnes, A., Schwark, I., Rothkirch, A.,
572 Tischer, M., Heuer, J., Schulte-Schrepping, H., Kracht, T., and Franz, H. (2015) The
573 Extreme Conditions Beamline P02.2 and the Extreme Conditions Science Infrastructure
574 at PETRA III. Journal of Synchrotron Radiation, 22(4), 908-924.
575 Lin, F., Hilairet, N., Raterron, P., Addad, A., Immoor, J., Marquardt, H., Tomé, C.N., Miyagi, L.,
576 and Merkel, S. (2017) Elasto-viscoplastic self consistent modeling of the ambient
577 temperature plastic behavior of periclase deformed up to 5.4 GPa. Journal of Applied
578 Physics, 122(20), 205902.
579 Lin, J.-F., Speziale, S., Mao, Z., and Marquardt, H. (2013) Effects of the Electronic Spin
580 Transitions of Iron in Lower Mantle Minerals: Implications for Deep Mantle Geophysics
581 and Geochemistry. Reviews of Geophysics, 51(2), 244-275.

582 Lin, J.-F., Struzhkin, V.V., Jacobsen, S.D., Hu, M.Y., Chow, P., Kung, J., Liu, H., Mao, H.-K.,
583 and Hemley, R.J. (2005) Spin transition of iron in magnesiowüstite in the Earth's lower
584 mantle. Nature, 436(7049), 377-380.
585 Marquardt, H., Buchen, J., Mendez, A.S.J., Kurnosov, A., Wendt, M., Rothkirch, A., Pennicard,
586 D., and Liermann, H.P. (2018) Elastic Softening of $(Mg_{0.8}Fe_{0.2})O$ Ferropericlase Across
587 the Iron Spin Crossover Measured at Seismic Frequencies. Geophysical Research Letters,
588 45(14), 6862-6868.
589 Marquardt, H., Speziale, S., Reichmann, H.J., Frost, D.J., and Schilling, F.R. (2009) Single-
590 crystal elasticity of $(Mg_{0.9}Fe_{0.1})O$ to 81 GPa. Earth and Planetary Science Letters, 287(3-
591 4), 345-352.
592 Marquardt, H., and Thomson, A.R. (2020) Experimental elasticity of Earth's deep mantle.
593 Nature Reviews Earth & Environment, 1(9), 455-469.
594 McCammon, C.A., Peyronneau, J., and Poirier, J.-P. (1998) Low ferric iron content of (Mg,Fe)O
595 at high pressures and temperatures. Geophysical Research Letters, 25(10), 1589-1592.
596 Méndez, A.S.J., Marquardt, H., Husband, R.J., Schwark, I., Mainberger, J., Glazyrin, K.,
597 Kurnosov, A., Otzen, C., Satta, N., Bednarcik, J., and Liermann, H.P. (2020) A
598 resistively-heated dynamic diamond anvil cell (RHdDAC) for fast compression x-ray
599 diffraction experiments at high temperatures. Review of Scientific Instruments, 91,
600 073906.
601 Méndez, A.S.J., Stackhouse, S., Trautner, V., Wang, B., Satta, N., Kurnosov, A., Husband, R.,
602 Glazyrin, K., Liermann, H.P., and Marquardt, H. (2022) Broad elastic softening of
603 (Mg,Fe)O ferropericlase across the iron spin crossover and a mixed-spin lower mantle.
604 Journal of Geophysical Research: Solid Earth, 127(8), e2021JB023832.

605 Miyagi, L. (2021) Experimental Deformation of Lower Mantle Rocks and Minerals. In H.
606 Marquardt, M.D. Ballmer, S. Cottaar, and J. Konter, Eds. Mantle Convection and Surface
607 Expressions, p. 21-50. American Geophysical Union, Washington, DC.
608 Miyagi, L., and Wenk, H.-R. (2016) Texture development and slip systems in bridgmanite and
609 bridgmanite + ferropericlase aggregates. Physics and Chemistry of Minerals, 43(8), 597-
610 613.
611 Mosca, I., Cobden, L., Deuss, A., Ritsema, J., and Trampert, J. (2012) Seismic and mineralogical
612 structures of the lower mantle from probabilistic tomography. Journal of Geophysical
613 Research: Solid Earth, 117, B06304.
614 Nestola, F., Nimis, P., Ziberna, L., Longo, M., Marzoli, A., Harris, J.W., Manghnani, M.H., and
615 Fedortchouk, Y. (2011) First crystal-structure determination of olivine in diamond:
616 Composition and implications for provenance in the Earth's mantle. Earth and planetary
617 science letters, 305(1), 249-255.
618 Prescher, C., and Prakapenka, V.B. (2015) DIOPTAS: a program for reduction of two-
619 dimensional X-ray diffraction data and data exploration. High Pressure Research, 35(3),
620 223-230.
621 Reuss, A. (1929) Berechnung der Fließgrenze von Mischkristallen auf Grund der
622 Plastizitätsbedingung für Einkristalle. Zeitschrift für angewandte Mathematik und
623 Mechanik, 9(1), 49-58.
624 Sinmyo, R., and Hirose, K. (2010) The Soret diffusion in laser-heated diamond-anvil cell.
625 Physics of the Earth and Planetary Interiors, 180(3-4), 172-178.
626 Solomatova, N.V., Jackson, J.M., Sturhahn, W., Wicks, J.K., Zhao, J., Toellner, T.S., Kalkan, B.,
627 and Steinhardt, W.M. (2016) Equation of state and spin crossover of (Mg,Fe)O at high

pressure, with implications for explaining topographic relief at the core-mantle boundary. American Mineralogist, 101(5), 1084-1093.

Stacey, F.D., Brennan, B.J., and Irvine, R.D. (1981) Finite strain theories and comparisons with seismological data. Geophysical Surveys, 4(3), 189-232.

Stixrude, L., and Lithgow-Bertelloni, C. (2024) Thermodynamics of mantle minerals – III: the role of iron. Geophysical journal international, 237(3), 1699-1733.

Toby, B.H., and Von Dreele, R.B. (2013) *GSAS-II*: the genesis of a modern open-source all purpose crystallography software package. Journal of Applied Crystallography, 46(2), 544-549.

Trautner, V.E., Rijal, A., Plueckthun, C., Satta, N., Koemets, E., Buchen, J., Wang, B., Glazyrin, K., Cobden, L., and Marquardt, H. (2024) Iron Content-Dependence of Ferropericlase Elastic Properties Across the Spin Crossover From Novel Experiments and Machine Learning. Geophysical Research Letters, 51(22), e2024GL111276.

Trautner, V.E., Stackhouse, S., Turner, A.R., Koelemeijer, P., Davies, D.R., Méndez, A.S.J., Satta, N., Kurnosov, A., Liermann, H.-P., and Marquardt, H. (2023) Compressibility of ferropericlase at high-temperature: Evidence for the iron spin crossover in seismic tomography. Earth and Planetary Science Letters, 618, 118296.

Voigt, W. (1928) Lehrbuch der Kristallphysik. Teubner, Leibzig.

Wang, B., Buchen, J., Méndez, A.S.J., Kurnosov, A., Criniti, G., Liermann, H.P., and Marquardt, H. (2023) Strong Effect of Stress on the Seismic Signature of the Post-Stishovite Phase Transition in the Earth's Lower Mantle. Geophysical Research Letters, 50(10).

Wang, B., Satta, N., Koemets, E., Buchen, J., Trautner, V., Méndez, A.S.J., Criniti, G., Glazyrin, K., Liermann, H.-P., and Marquardt, H. (2026) Dynamic compression and pressure

cycling in dynamic diamond anvil cells: MgO and neon studied by time-resolved x-ray diffraction. Physical Review B.

Watt, J.P., Davies, G.F., and O'Connell, R.J. (1976) The elastic properties of composite materials. Reviews of geophysics, 14(4), 541-563.

Wolf, A.S., Jackson, J.M., Dera, P., and Prakapenka, V.B. (2015) The thermal equation of state of (Mg, Fe)SiO_3 bridgmanite (perovskite) and implications for lower mantle structures. Journal of Geophysical Research: Solid Earth, 120(11), 7460-7489.

Wu, Z., Justo, J.F., and Wentzcovitch, R.M. (2013) Elastic anomalies in a spin-crossover system: ferropericlase at lower mantle conditions. Physical Review Letters, 110, 228501.

Figure Captions

Figure 1. Representative X-ray diffraction patterns of the bridgmanite-periclase polycrystal at different experimental conditions. Calculated (calc) spectra from LeBail fitting are also shown, with subtracted background (bkg) and difference curve (diff), as well as the differences between measured and calculated spectra divided by their uncertainty (Δ/σ). **(a)** Sample in air at ambient pressure and temperature. **(b)** Unannealed sample in helium, at 51 GPa and 300 K. **(c)** Annealed sample in KCl, at 51 GPa and 300 K.

Figure 2. Backscattered electron images (top-row) and EDS elemental maps acquired at 5 kV for Si, Mg and Fe (second, third and fourth row, respectively) of cross-sections of the laser-heated areas in the polycrystalline sample of bridgmanite and periclase. Bridgmanite appears darker in the BSE images, while periclase appears brighter. The compression axis during the experiment is indicated by the black arrow on the right. **(a)** Cross-section of spot 2, which was heated at 2200 K (outlined by the red ellipse). The black ellipse indicates an area enriched in aluminum. **(b)** Cross-section of spot 1, which was heated at 1800 K (outlined by the red ellipse).

Figure 3. Compression curves for **(a)** periclase (blue circles) and **(b)** bridgmanite (red diamonds). Volume-pressure data collected during compression of the two-phase sample in KCl or in helium as pressure medium and with or without laser-annealing are shown with filled and open symbols, respectively. The open star indicates the volumes at ambient conditions and the filled star indicates volumes measured in KCl before annealing. Also shown are literature data with similar compositions as those estimated for the two-phase sample: **(a)** single-phase powder of Fe-bearing periclase as filled (Marquardt et al. 2009) and open (Lin et al. 2005) black triangles, as well as theoretical computations (Trautner et al. 2023) (black line); **(b)** single-crystal bridgmanite (Boffa Ballaran et al. 2012) and single-phase powder of bridgmanite (Catalli et al. 2010) as filled and open black squares, respectively.

Figure 4. Schematic representation of the differences in compression behavior of a sintered bridgmanite-periclase polycrystal with and without high-temperature stress annealing. Bridgmanite (Bg, red) forms a load-bearing framework, shielding periclase (Per, blue) from the external pressure (P_{Ext}) during compression without annealing **(top right)**. Because the relative volume change ($\Delta V/V_{ref}$) in bridgmanite and periclase is the same, but periclase is more compressible, this results in a lower pressure acting on the periclase grains. During compression with annealing **(bottom right)**, pressure is homogenized, resulting in a larger volume reduction in periclase with respect to bridgmanite. The dashed lines indicate the pre-compression state of the grains.

Figure 5. Volume strain as a function of pressure for periclase (blue circles) and bridgmanite (red diamonds) in the sintered polycrystal, relative to the volume at 27 GPa. Strains measured in the experiments with or without laser-annealing are shown as filled and open symbols, respectively. Also shown are literature data for single-phase powder of Fe-bearing periclase as

filled (Marquardt et al. 2009) and open (Lin et al. 2005) black triangles, as well as single-crystal bridgmanite (Boffa Ballaran et al. 2012) and single-phase powder of bridgmanite (Catalli et al. 2010) as filled and open black squares, respectively. The black line shows theoretical computations for Fe-bearing periclase (Trautner et al. 2023).

Figure 6. Normalized stress *F* as a function of pressure for $(Mg_{1-x}Fe_x)O$ periclase. Data from periclase in the two-phase sample with and without laser-annealing are shown with filled and open blue circles, respectively. Also shown are literature data for single-phase periclase from Marquardt et al. (2009) (filled black triangles) and Lin et al. (2005) (open black triangles), as well as theoretical computations (Trautner et al. 2023) (black line). A drop in the normalized stress occurs across the pressure range of the iron spin crossover, which is indicated as filled and open bars for the experiments with and without laser-annealing, respectively.

709 **Figures**

710

Figure 1

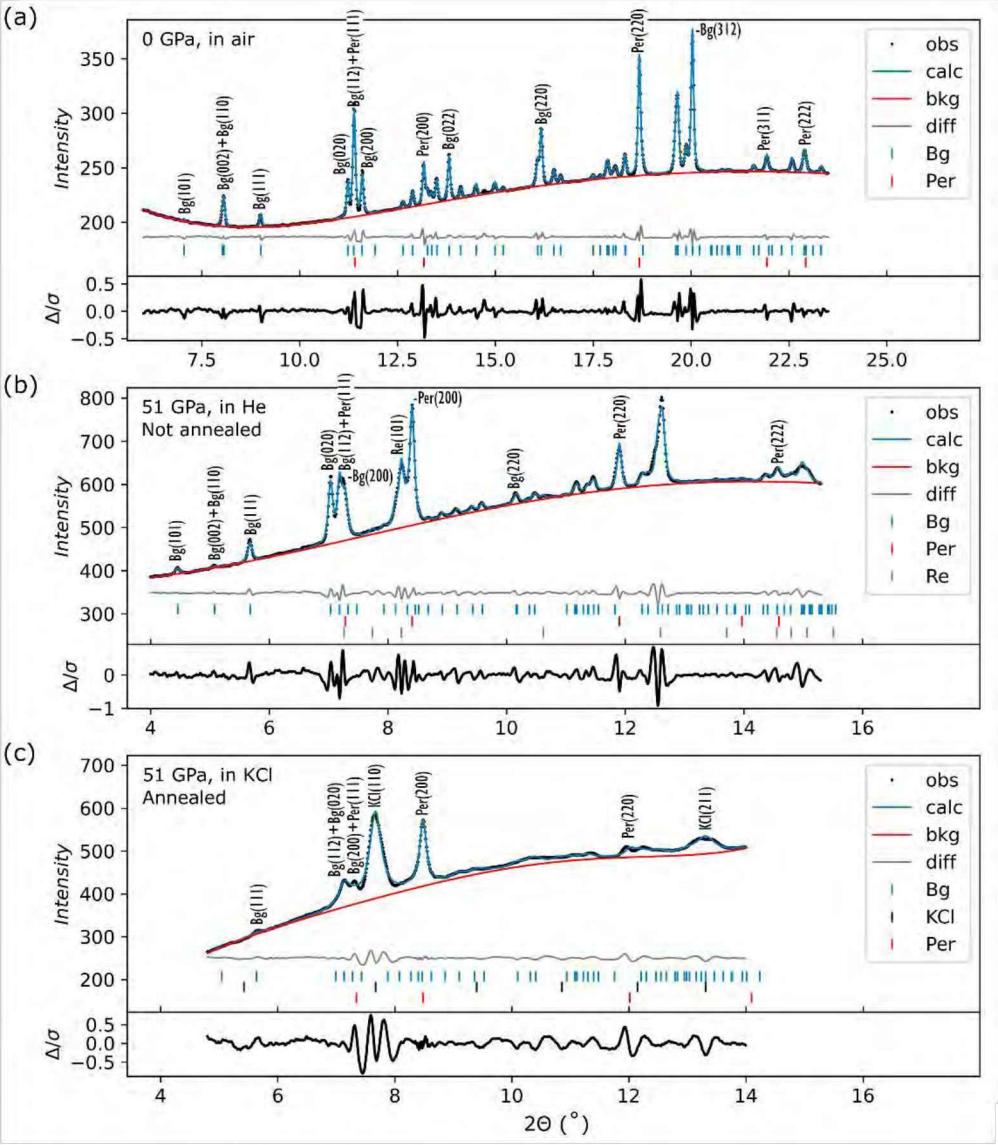

711

712

713

714

This is the peer-reviewed, final accepted version for American Mineralogist, published by the Mineralogical Society of America.
The published version is subject to change. Cite as Authors (Year) Title. American Mineralogist, in press.
DOI: https://doi.org/10.2138/am-2025-10040. http://www.minsocam.org/

715 Figure 2

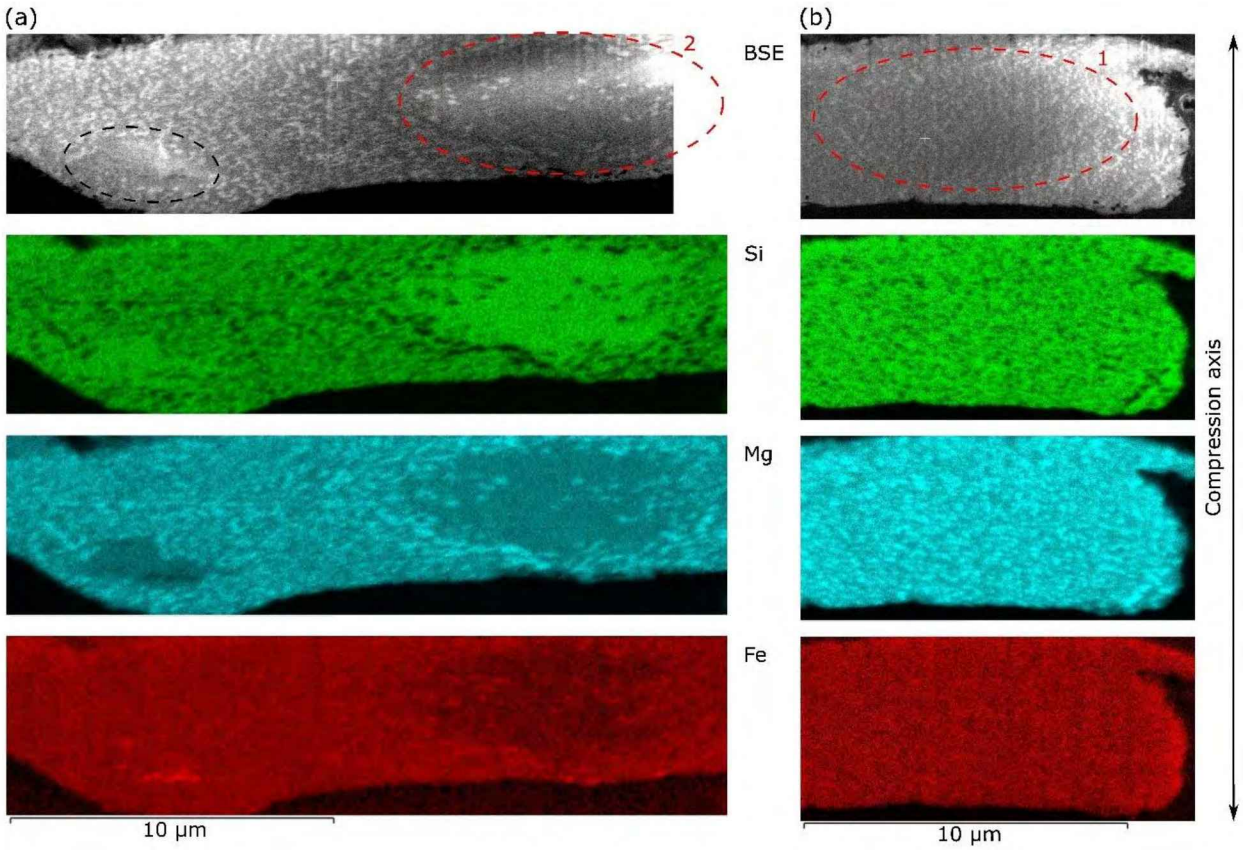

716

Figure 3

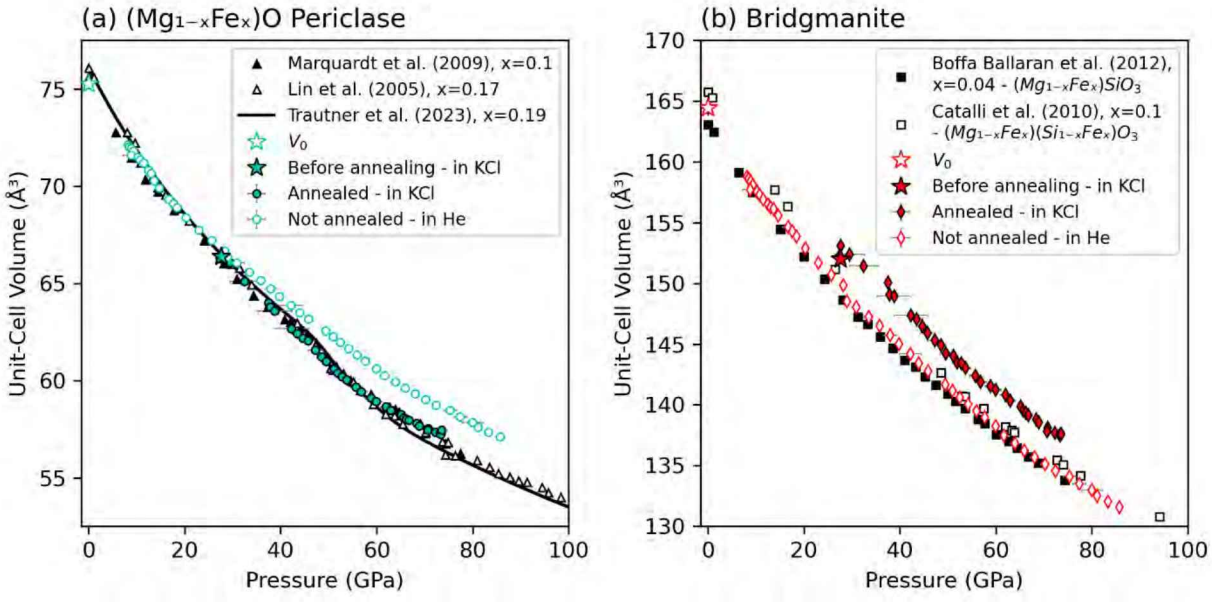

717

This is the peer-reviewed, final accepted version for American Mineralogist, published by the Mineralogical Society of America.
The published version is subject to change. Cite as Authors (Year) Title. American Mineralogist, in press.
DOI: https://doi.org/10.2138/am-2025-10040. http://www.minsocam.org/

Figure 4

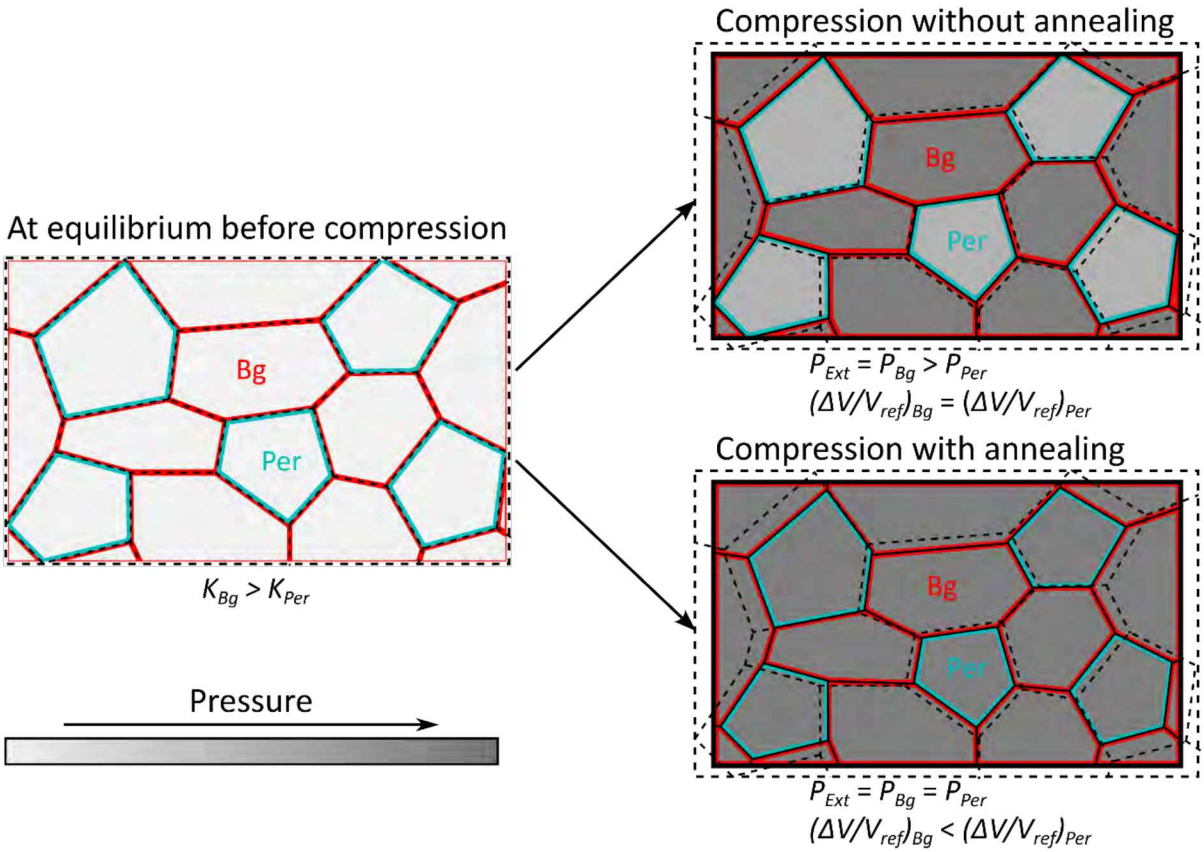

718

719

This is the peer-reviewed, final accepted version for American Mineralogist, published by the Mineralogical Society of America.
The published version is subject to change. Cite as Authors (Year) Title. American Mineralogist, in press.
DOI: https://doi.org/10.2138/am-2025-10040. http://www.minsocam.org/

Figure 5

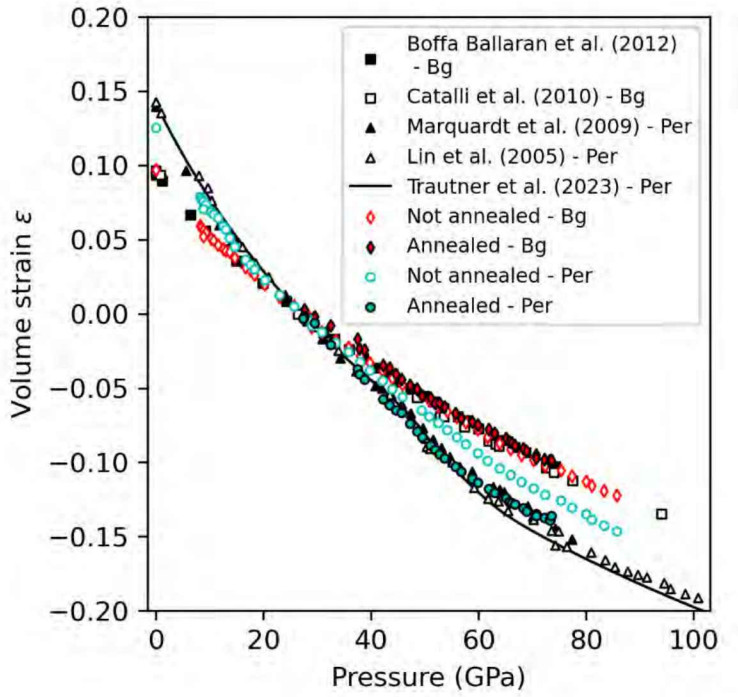

720

721 Figure 6

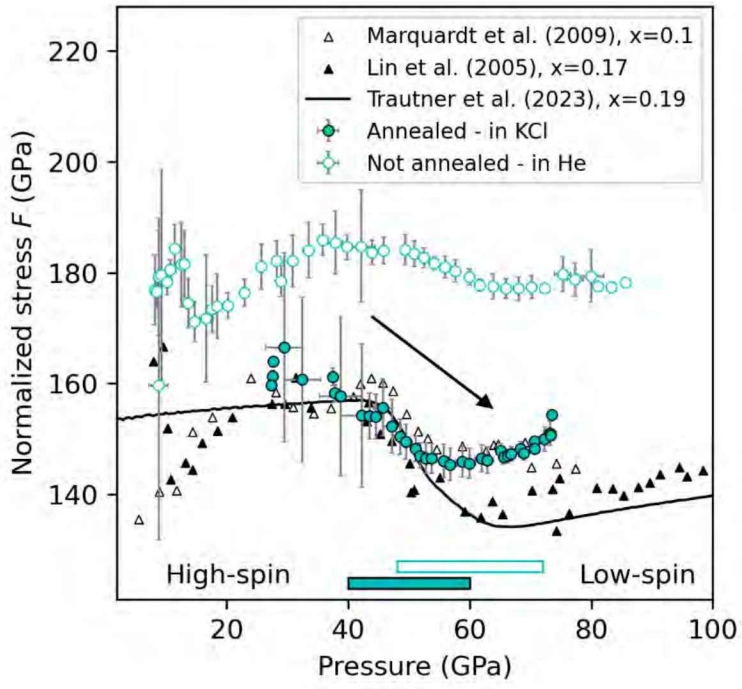

722